In-situ synchrotron X-ray diffraction investigation of microstructure evolution in Cr-doped cemented carbide during high-temperature creep

International Journal of Refractory Metals and Hard Materials 141 (2026) 108016

Contents lists available at ScienceDirect

International Journal of Refractory Metals and Hard Materials

journal homepage: www.elsevier.com/locate/IJRMHM

In-situ synchrotron X-ray diffraction investigation of microstructure evolution in Cr-doped cemented carbide during high-temperature creep deformation☆

Ahmet Bahadir Yildiz [a,*], Anna Böhm [b], Ida Borgh [b], Abdalrhaman Koko [c], Christina Reinhard [d,e], Štefan Michalik [f], Emil Österberg [a], Stefan Olovsjö [g], Mikael Kritikos [h], Fredrik Lindberg [h], Jonathan Weidow [i], Susanne Norgren [b,h,j], Peter Hedström [k,*]

[a] Scatterin AB, Drottning Kristinas väg 53, 114 28 Stockholm, Sweden
[b] Sandvik Mining, R&D Rock Tools, 126 80 Stockholm, Sweden
[c] National Physical Laboratory, Hampton Road, Teddington TW11 0LW, UK
[d] The University of Manchester at Harwell, Diamond Light Source, Didcot OX11 0DE, UK
[e] The University of Manchester, Faculty of Science and Engineering, Oxford Road, Manchester M13 9PL, UK
[f] Diamond Light Source Ltd., Harwell Science and Innovation Campus, Didcot OX11 0DE, UK
[g] Seco Tools AB, R&D Materials and Technology, 737 82 Fagersta, Sweden
[h] Sandvik Coromant R&D, SE-126 80 Stockholm, Sweden
[i] Department of Physics, Chalmers University of Technology, 412 96 Göteborg, Sweden
[j] Department of Mechanical Engineering, Lund University, 223 62 Lund, Sweden
[k] Dept. of Materials Science and Engineering, KTH Royal Institute of Technology, 100 44 Stockholm, Sweden

ARTICLE INFO

Keywords:
WC-Co
Cr
High-temperature
Hard metals
Synchrotron x-ray diffraction (SXRD)
In-situ
Compression test

ABSTRACT

This study investigates the high-temperature mechanical response of plain and Cr-doped WC-Co cemented carbides using in-situ synchrotron X-ray diffraction (S-XRD) during electro-thermomechanical testing at 1000 °C under compressive stresses up to 900 MPa. The results show that the Co-rich binder phase in the Cr-doped material is exposed to higher tensile stresses during deformation than in the undoped system, indicating modified load partitioning between WC and the binder. Furthermore, the WC phase in the Cr-doped material carries significantly higher compressive stresses, reaching ~230 MPa higher compressive stress at the same macroscopic deformation compared to the plain WC-Co sample. These findings suggest that Cr-doping alters load transfer and phase-specific stress evolution, resulting in enhanced high-temperature deformation properties, i.e. improved creep resistance. This improvement is likely linked to solid solution strengthening in the binder and modified WC/Co and WC/WC interface chemistry.

1. Introduction

WC-Co cemented carbides are widely used as tool materials in metal cutting and rock drilling applications due to their excellent wear resistance, high hardness, and good fracture toughness. During service in metal cutting, these tools are subjected to high mechanical stresses while simultaneously experiencing temperatures that can reach up to 1100 °C. Under such extreme conditions, several deformation and degradation mechanisms; including creep deformation, binder diffusion, dissolution and re-precipitation of WC, and grain boundary sliding, may contribute to progressive tool damage and eventual tool failure.

Previous studies have demonstrated that Cr additions to the WC-Co cemented carbides enhance high-temperature resistance to plastic deformation and improve toughness [1–5]. For example, the investigation of high-temperature creep in plain and Cr-doped WC-Co cemented carbides of comparable average WC grain size has shown over 2.5-fold increase in deformation resistance at 1000 °C under a compressive stress of 900 MPa [6]. The authors also reported that WC grain coarsening occurred in the direction perpendicular to the loading direction, whereas grain size remained unchanged parallel to the loading

☆ This article is part of a Special issue entitled: 'Plansee 2025' published in International Journal of Refractory Metals and Hard Materials.

* Corresponding authors.
E-mail addresses: ahmet@scatterin.com (A.B. Yildiz), pheds@kth.se (P. Hedström).

https://doi.org/10.1016/j.ijrmhm.2026.108016
Received 31 January 2026; Received in revised form 12 July 2026; Accepted 22 July 2026
Available online 23 July 2026

direction. This anisotropic coarsening is attributed to the dissolution of smaller WC grains during high temperature deformation, potentially combined with preferential dissolution of WC interfaces aligned with the loading direction and growth in the perpendicular direction [3]. Furthermore, binder redistribution leads to infiltration of the Co-rich binder phase between WC grains, contributing further to grain coarsening. This binder infiltration, combined with cavity formation, suggests that WC grain boundary sliding plays a role in the deformation process. Moreover, previous transmission electron microscopy (TEM) studies have revealed an increased dislocation density in both the WC and Co-rich binder phase [5].

The enhanced creep resistance in Cr-doped cemented carbides can be attributed to multiple mechanisms occurring simultaneously. Alloying the Co-rich binder phase with Cr results in solid solution hardening, which can alter strain partitioning and influence the evolution of dislocation densities during deformation. Such hardening has been shown to improve creep resistance in cemented carbide grades with relatively high binder content [7]. Increased dislocation content in WC can subsequently serve as nucleation sites for WC grain growth during high-temperature deformation. Furthermore, first-principles calculations have shown that the addition of Cr lowers the stacking fault energy of FCC Co-rich binder phase, stabilizing the HCP Co-rich phase [8]. Previous studies have also shown that Cr-doping results in Cr segregation on WC/Co phase and WC/WC grain boundaries which can strengthen the WC/WC boundaries and increase the work of separation important for binder infiltration [9,10]. Cr-doping has also been linked to higher WC contiguity and an increased fraction of Σ2 boundaries, at which Co segregation was reported to be energetically unfavourable [9,11,12]. Furthermore, Σ2 boundaries have been measured to have lower fracture energy than transgranular cleavage on prismatic planes, indicating an energetically favourable crack path along these boundaries [13].

Although multiple theories have been proposed, the structural evolution during service and the mechanism by which Cr-doping enhances performance remain unclear, limiting further product development. A full understanding of the mechanisms governing the microstructural evolution during service is only possible by additional in-situ or operando experiments. Hence, in this work, we perform in-situ synchrotron X-ray diffraction experiments using an Instron electro-thermomechanical test rig (ETMT) [14] at 1000 °C under compressive stress up to 900 MPa and probe the mechanical response of WC and Co-rich binder phase in plain and Cr-doped cemented carbides of similar average WC grain size.

2. Materials and methods

Two as-sintered WC-6 wt% Co cemented carbide materials, one reference (WC-Co) and one with 0.6 wt% Cr addition (WC-Co-Cr), were used for these investigations. The two cemented carbide materials were produced through standard powder metallurgical methods including milling, drying, pressing, and sintering. The powders were pressed into a geometry of 54 mm long beams and then gas-pressure-sintered at 1410 °C for 1 h under 55 bar Argon pressure. The processing route was designed to produce materials with similar microstructure, enabling a comparison of the effect of Cr-doping on deformation without considering the WC grain growth inhibition effect that often is seen in Cr-doped materials. To achieve this, WC powders with different initial particle sizes were used to compensate for the grain growth inhibiting effect of Cr.

The specimens suitable for the ETMT measurements were prepared by electrical discharge machining (EDM) into a dog bone shape with a waist cross-section of 1×1 mm^2.

Following the sintering process, standard magnetic property measurements, including coercivity and relative magnetic saturation measurements, were performed on both materials. In addition, hardness was determined by performing Vickers hardness tests with a 20 kg load, applying five indents and evaluating an average of these measurements.

2.1. Equilibrium thermodynamic calculations

Thermodynamic calculations were performed using Thermo-Calc software with the TCFE14 database [15], which, despite being assessed for steels, includes data relevant to cemented carbide systems. The equilibrium calculations were performed to show how Cr-doping affects the thermodynamics of the cemented carbide system. The calculations were performed in the same way as described in [16]. For both systems, some phases were excluded from the calculations. M_3C_2 and M_3C were excluded since it is experimentally known that M_7C_3 and graphite will form instead of M_3C_2 (where M = Cr,W) and M_3C (where M = W, Co). W_2C was excluded as it has never been experimentally identified.

Isopleths were evaluated for both systems to investigate phase stability. Based on [17], atom mobility is considered limited below 1000 °C, thus phases and binder composition are assumed to remain constant below this temperature. This assumption was applied by calculating phase stability and binder composition for the two systems at 1000 °C.

2.2. Scanning electron microscopy (SEM) and electron backscatter diffraction (EBSD)

The structure of the two materials was investigated using observations from SEM micrographs and by using EBSD analysis of WC grain size, distribution and boundary characteristics as well as binder structure and binder pocket size. The microstructure is important in this work since it will affect how the internal stresses are distributed within the material.

Sample preparation for the sintered materials was conducted using standard methods, including cutting, grinding and mechanical polishing down to 1 μm diamond suspension. Additionally, broad Ar^+ ion beam polishing was performed in two steps. First at 6.0 kV for 90 min and second at 2.0 kV for 20 min in a Hitachi IM4000 system using an incidence angle of 4°.

Microscopy and EBSD analysis were performed using a Jeol JSM-7800F scanning electron microscope equipped with an Oxford Instrument, Symmetry S3 EBSD detector. For EBSD acquisition, the AZtec software was used, and EBSD maps of 160 × 120 μm were collected using an acceleration voltage of 20 kV and a step size of 0.1 μm. For post-processing, the data was exported to the MTEX toolbox [18] and evaluated using the following criteria: WC-WC boundaries were defined as having a misorientation angle larger than 3 degrees and boundaries were closed. Grains located at the boundary of the map were excluded; The minimum grain size was defined as 4 pixels in area. Pseudo-symmetries were handled by removing misindexed orientations related by a 30 degrees rotational pseudosymmetry around the [0001] axis for WC, using an allowed deviation angle of 5 degrees. All zero solutions (less than 1% of the total map) were then filled using the fill algorithm in MTEX. Phase statistics were extracted from the cleaned data.

To evaluate the contiguity, WC grain boundaries, phase boundaries WC-Co FCC, and WC-Co HCP, were first evaluated. Then, WC-WC contiguity was evaluated using the following expression (Eq. 1):

$$C_{WC-WC} = \frac{2L_{WC-WC}}{2L_{WC-WC} + L_{WC-Co\ FCC} + L_{WC-Co\ HCP}} \quad (1)$$

where $L_{WC\text{-}WC}$ is the total WC/WC grain boundary length in μm, while $L_{WC\text{-}Co\ FCC}$ and $L_{WC\text{-}Co\ HCP}$ are the WC/binder phase boundary lengths for the FCC and HCP Co-rich binder phases, respectively. This expression is in line with the work in [19]. However, both grain and phase boundary lengths are here taken from the EBSD data. Σ2 special boundaries were defined by a 90-degree rotation about the [10−10] axis, with an angular

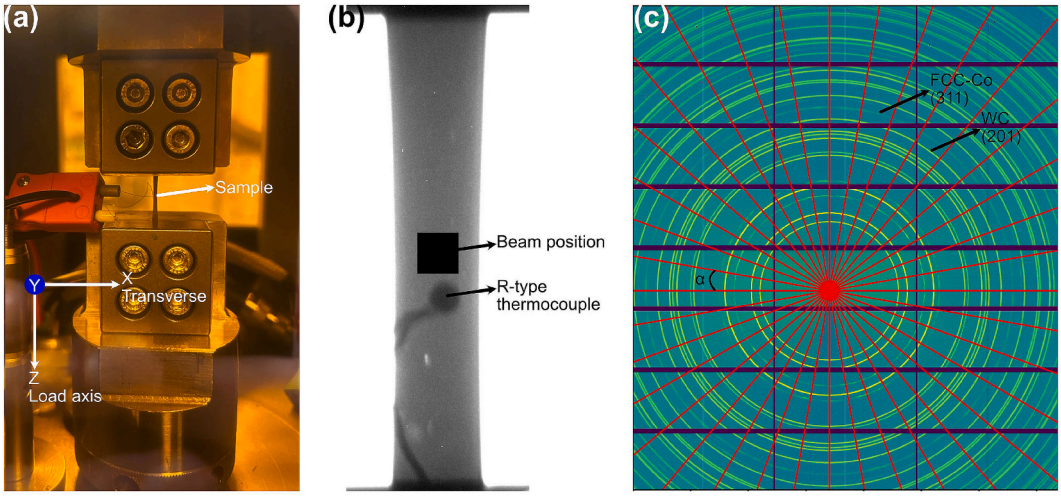

Fig. 1. (a) Experimental setup for in-situ synchrotron X-ray diffraction during electro-thermomechanical testing, showing the sample position and the transverse (X) and axial/loading (Z) directions. (b) Synchrotron radiograph of the sample in the gauge section, showing the beam position and the R-type thermocouple attachment. The incident X-ray beam propagated along the Y direction through the sample thickness. (c) Representative 2D detector image acquired in transmission geometry, showing Debye–Scherrer rings from the WC and FCC Co-rich binder phases used for strain analysis; azimuthal sectors with azimuthal angle (α) used to determine the angle-dependent lattice strain are indicated schematically.

tolerance of 5 degrees.

To characterize the grain size distribution, D10, D50 and D90 were used. In accordance with [20], these were defined as the equivalent diameter dN for which the cumulative area fraction of grains with equivalent diameter smaller or equal to dN reaches 10%, 50%, or 90% of the total measured grain area, i.e.

$$\frac{\sum_1^N A_i}{\sum_1^M A_i} = 0.10, 0.50, or\ 0.90 \tag{2}$$

where A_i is the area of grain i, the grains are ordered by increasing equivalent diameter, and M is the total number of measured grains. D50 is used as the mean grain size, and D90-D10 represents the width of the grain size distribution.

2.3. In-situ synchrotron X-ray diffraction (S-XRD)

In-situ S-XRD experiments were performed in transmission geometry on the I12 (JEEP) beamline [21] at Diamond Light Source in the UK, using a monochromatic X-ray beam with a wavelength of 0.18106 Å (68.478 keV). An INSTRON 3 kN ETMT was used for high temperature deformation experiments. The temperature was controlled by an R-type thermocouple attached to the sample. Fig. 1.a shows the placement of a sample and connection of the R-type thermocouple to the ETMT. A synchrotron X-ray radiograph of a sample in Fig. 1.b shows the spot welding of the R-type thermocouple in the centre of the sample and the positioning of the X-ray beam with a spot size of 0.5 mm × 0.5 mm. The incident beam was aligned along the Y direction, i.e. normal to the sample surface shown in Fig. 1.a and penetrated through the full sample thickness of 1 mm at the gauge section. The diffracted X-rays formed Debye–Scherrer cones that were recorded by a Pilatus3 X CdTe 2M area detector positioned behind the sample. A representative detector image is shown in Fig. 1c. S-XRD data were collected at 3 s/pattern data acquisition rate and used for phase identification and strain analysis.

Macroscopic displacement was obtained from the ETMT cross-head movement. Samples were heated to 1000 °C with a 5 °C/s heating rate using resistance heating in an Ar atmosphere. Upon reaching 1000 °C, the load was equilibrated followed by a 150 N stepwise increase to 900 N compressive load (30 s ramping- and holding-time per step). The load was then kept constant for 10 min or until sample failure. In the current setup, the specimens were positioned so that the wide section aligned with the grips, and deformation was monitored through the crosshead displacement. The macroscopic strain (ε) is therefore obtained from the macroscopic displacement (ΔL) recorded by the ETMT and the initial gauge length between the sample grips, (L_0= 16 mm) according to:

$$\varepsilon = \Delta L/L_0 \tag{3}$$

It should be noted that the gauge section is not perfectly parallel but exhibits a slight taper (see Fig. 1a), and a temperature gradient is present within the gauge region due to the localized resistive heating characteristic of this setup.

A NIST Standard Reference Material (SRM 674b) CeO2 powder was used for the calibration of the experimental setup. The calibration of experimental setup, azimuthal integration of diffraction patterns, and residual strain/stress analysis were performed using the commercially available Scatterin SaaS data analysis software [22].

For phase-specific strain measurements, the (201) peak of hexagonal WC phase and (311) peak of face-centred cubic (FCC) Co-rich binder phase were used. The phase-specific lattice strain was calculated as a function of azimuthal angle (α), see Fig. 1.c, by:

$$\varepsilon_\alpha = \frac{sin\theta_0}{sin\theta_\alpha} - 1 \tag{4}$$

where, θ_α is the diffraction angle of either (201) WC or (311) Co-rich binder diffraction peaks at each azimuthal angle α, and θ_0 is the reference diffraction angle representing the value at zero applied stress. We used 36 equally spaced azimuthal bins. For each bin, θ_0 was determined from the corresponding azimuthally binned S-XRD data collected at 1000 °C prior to the application of external loading.

The determined azimuthal dependency of strain was then used to solve the strain tensor in a similar procedure as described in Ref. [23], providing the strain components ε_{XX} and ε_{ZZ} along the principal directions together with the shear component $\varepsilon_{XZ} = \varepsilon_{ZX}$. We employed the full 3D Hooke's law in its Lamé formulation, assuming $\sigma_{XX} = \sigma_{YY}$ for the principal stresses and $\tau_{XZ} = \tau_{YZ}$ with $\tau_{XY} = 0$ for the shear stresses. These constraints represent a triaxial stress configuration with biaxial symmetry in the plane:

$$\varepsilon_\parallel = \varepsilon_{XX} = \varepsilon_{YY} \tag{5}$$

$$\sigma_{XX} = \sigma_{YY} = [E_{hkl}/((1+\nu)(1-2\nu))][\varepsilon_\parallel + \nu\varepsilon_{zz}] \tag{6}$$

Table 1
Standard characteristic data.

Sample	Hardness HV20	Coercivity (kA/m)	Magnetic Saturation (Tm^3/kg)
WC-Co	1421 ± 5	10.85	96.26×10^{-7}
WC-Co-Cr	1449 ± 7	11.55	86.40×10^{-7}

$$\sigma_{ZZ} = [E_{hkl}/((1+\nu)(1-2\nu))][2\nu\varepsilon_{\parallel} + (1-\nu)\varepsilon_{zz}] \quad (7)$$

$$\tau_{XZ} = \tau_{YZ} = 2G\varepsilon_{xz} \quad (8)$$

where, E_{hkl} is the diffraction Young's modulus, 157.47 GPa for (311) FCC Co and 678.56 GPa for (201) WC, ν_{hkl} is the diffraction Poisson's ratio, 0.355 for (311) FCC Co and 0.231 for (201) WC, and G is the diffraction shear modulus. These diffraction elastic constants were calculated from room-temperature single-crystal elastic constants using the self-consistent Kröner–Eshelby model [24,25]. A previous study reported that the Young's modulus of WC decreases by only about 4% at 1000 °C compared to room temperature [26]. We thus use the room-temperature values for WC. For the Co-rich binder, single-crystal elastic constants are not available for relevant alloy compositions and temperatures. Therefore, we use the room-temperature values for FCC Co to evaluate phase-specific stresses.

3. Results

3.1. Materials

The hardness and magnetic property data for the two cemented carbide materials are presented in Table 1. The magnetic saturation is lower for the Cr-doped material, as expected, since Cr reduces the magnetic moment of the binder [27]. The coercivity value is also higher for the Cr doped material compared with the un-doped material. Further, the Cr-doped material shows slightly higher hardness compared with the un-doped material.

3.2. Equilibrium thermodynamic calculations

Fig. 2.a and b show the equilibrium phase diagram, or isopleth, of WC-Co and WC-Co-Cr cemented carbides, respectively. According to the isopleths in Fig. 2, the Cr addition influences the liquidus/solidus temperatures for the binder phase. Further, Cr addition effects the stable phases present in the cemented carbide, where M_7C_3 stabilizes at higher C contents. The C content range for the desired WC-Co-(M_7C_3) region at 1000 °C can be estimated from the C contents at the limits of the WC-Co-η region on the low-C side and the WC-Co-Graphite-(M_7C_3) region on the high-C side. As shown in Fig. 2b, Cr addition widens this carbon-content window compared with the undoped WC–Co system.

Single point equilibrium calculations at η and graphite limits show stable phases and their volume fractions, as well as the composition of the FCC Co-rich binder phase. The results are provided in Tables 2 and 3.

Depending on the C content for the system, the solubilities of W and C in the binder phase vary. Generally, the η phase limit is associated with higher W solubility and lower C solubility, while the graphite limit

Table 2
Calculated stable phase fractions at 1000 °C at the limit to η phase and graphite limits.

Carbon activity	System	Co FCC (vol. fr.)	M7C3 (Vol. fr.)	WC (vol. fr.)
η phase limit	WC-6w%Co	0.116	–	0.884
	WC-6w%Co-0.6w%Cr	0.130	–	0.870
Graphite limit	WC-6w%Co	0.108	–	0.892
	WC-6w%Co-0.6w%Cr	0.113	0.0116	0.876

Table 3
Calculated binder (FCC) composition at 1000 °C at the η phase and graphite limits.

Carbon activity	System	C (at. %)	W (at. %)	Cr (at. %)	Co (at. %)
η phase limit	WC-6w%Co	0.302	5.818	–	93.880
	WC-6w%Co-0.6w%Cr	0.585	5.692	9.541	84.182
Graphite limit	WC-6w%Co	1.220	0.449	–	98.331
	WC-6w%Co-0.6w%Cr	2.297	0.923	4.920	91.860

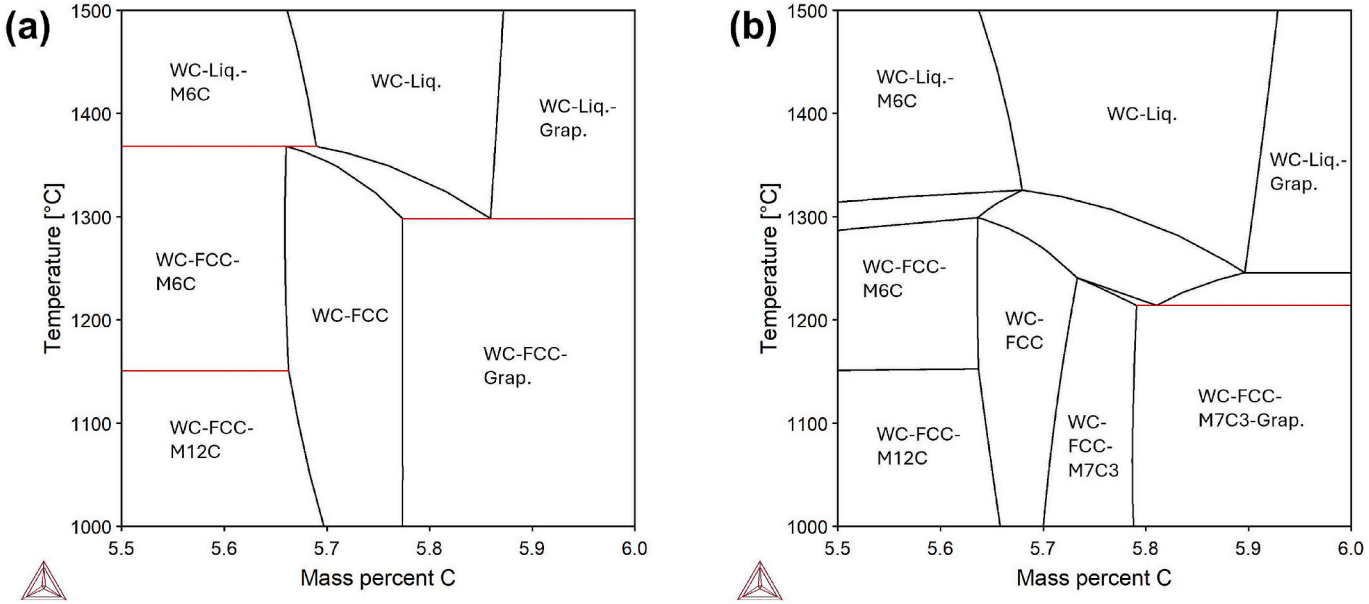

Fig. 2. Equilibrium phase diagrams of (a) WC–Co and (b) WC–Co–Cr cemented carbides.

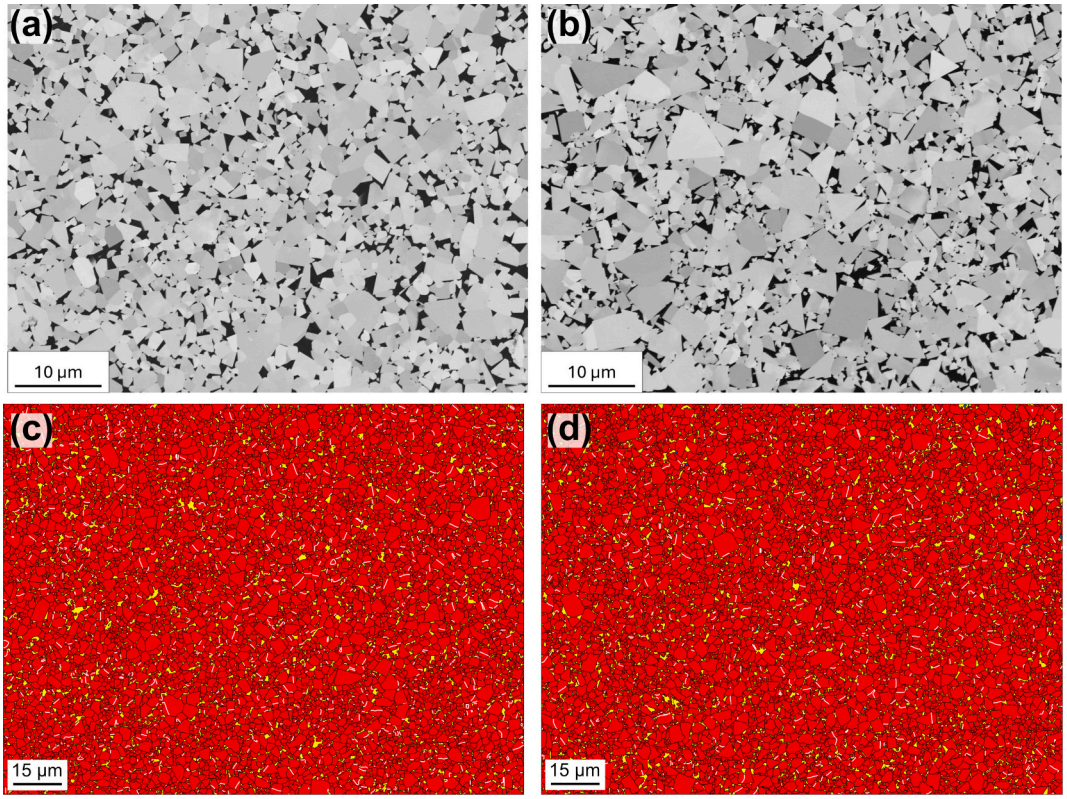

Fig. 3. SEM micrographs (a, b) and EBSD phase maps (c, d) of the as-sintered WC–Co and WC–Co–Cr cemented carbides: (a, c) WC–Co and (b, d) WC–Co–Cr. In the phase maps, red and yellow correspond to the WC and FCC Co-rich binder phases, respectively, while Σ2 boundaries are marked in white. (For interpretation of the references to colour in this figure legend, the reader is referred to the web version of this article.)

exhibits the opposite trend; this can also be seen in the equilibrium thermodynamic calculation results. The increased W solubility at the η phase limit largely accounts for the higher volume of the binder phase seen for both systems at this limit. Further, the Cr addition will result in a larger volume of the binder phase compared to the un-doped system at both limits. Additionally, changes in the volume fraction between the η phase and graphite limits are also related to the formation of M_7C_3 when more C is present.

The composition of the binder phase is notably influenced by the addition of Cr. When Cr is introduced to the system, there is an increase in C solubility at both the η phase and graphite limits. At the η phase limit the W solubility is rather equal for the two systems. However, for the Cr doped system, in addition to the W, a large fraction of Cr has dissolved in the binder phase. This results in a binder with a much higher amount of substitutional atoms dissolved compared with the un-doped system. At the graphite limit, the addition of Cr results in a higher W solubility within the binder phase compared to the un-doped system. Here also a large fraction of Cr is dissolved, however, at a lower level than at the η phase limit due to the formation of M_7C_3. Nevertheless, the overall fraction of substitutional atoms in the binder remains larger for the Cr-doped system than for the system without Cr, both at the η phase and graphite limits.

Both investigated samples are within the target WC-Co or WC-Co-M_7C_3 regions, hence, the phase fraction and binder phase composition are expected to be between these limits.

3.3. SEM and EBSD

SEM micrographs of the two materials are presented in Fig. 3.a and b. According to the micrographs, neither η phase nor graphite is observed, as expected. The overall structures are very similar for the two materials. Phase-coloured maps obtained from EBSD analysis are shown in Fig. 3.c and d, illustrating an FCC-dominated Co-rich binder structure in both samples. Statistics relating to WC grain size are provided in Table 4.a. Comparing the two materials, only small differences can be noted, The WC-Co-Cr material shows a slightly larger grain size and lower contiguity. Further, a small difference in the fraction of Σ2 boundaries over all WC grain boundaries can be seen where the WC-Co material has a higher fraction compared to the WC-Co-Cr material.

From the EBSD analysis, the binder pocket size can also be evaluated. This does not represent the true binder grain size, which extends across larger regions of the structure as can be seen in [28]. Binder pocket size statistics are listed in Table 4.b. Comparing the two materials, a higher binder area fraction is observed for the WC-Co-Cr material, as expected since Cr dissolves in the binder phase and causes increased binder volume fraction. The WC-Co material indicates a slightly larger binder

Table 4
EBSD results on microstructural statistics.

(a) WC grain size statistics

Sample	No. of grains	D10 (µm)	D50 (µm)	D90 (µm)	D90-D10 (µm)	C_{WC-WC}	Σ2 fraction [%]
WC-Co	9442	1.0	2.1	3.7	2.7	0.64	7.92
WC-Co-Cr	9144	1.0	2.3	3.9	2.9	0.59	5.94

(b) FCC binder pocket size statistics

Sample	No. of pockets	D10 (µm)	D50 (µm)	D90 (µm)	D90-D10 (µm)	Binder area fraction [%]
WC-Co	3441	0.5	1	1.9	1.4	7.3
WC-Co-Cr	4045	0.4	0.9	1.7	1.3	8.0

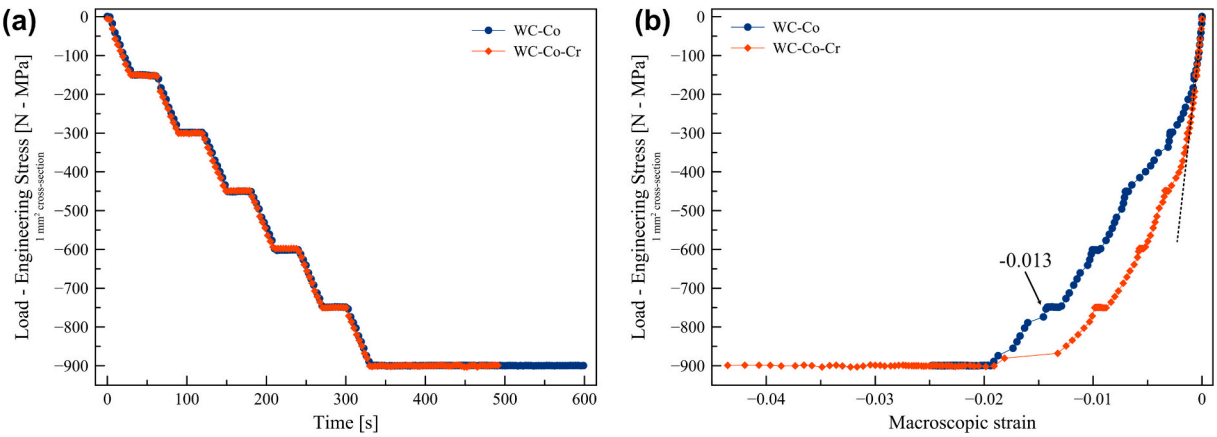

Fig. 4. Engineering stress–time (a) and engineering stress–strain (b) curves for WC–Co and WC–Co–Cr cemented carbides at 1000 °C, recorded by the ETMT device during the in-situ S-XRD experiments.

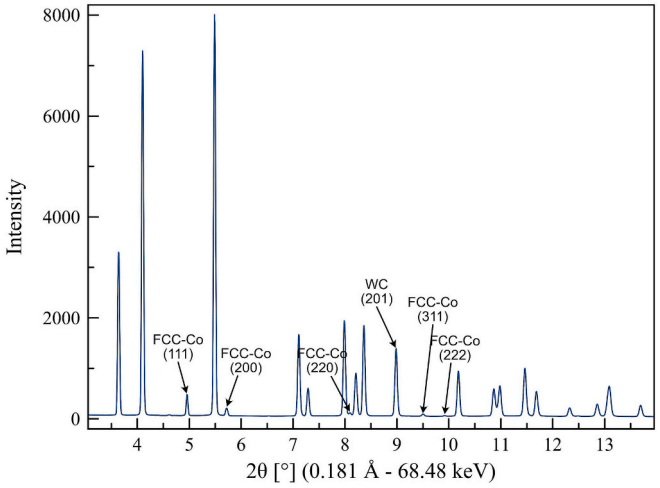

Fig. 5. Typical S-XRD pattern (full azimuthal integration) of WC–Co cemented carbide acquired at 1000 °C in this work. Five different reflections from the FCC Co-rich binder phase are highlighted.

pocket size, but the differences are small; this relates also to the small differences seen in contiguity for the two materials.

3.4. *In-situ synchrotron X-ray diffraction (S-XRD)*

Fig. 4.a and b show engineering stress-time and engineering stress-macroscopic strain curves of WC-Co and WC-Co-Cr cemented carbides at 1000 °C. As seen in Fig. 4.a, the samples are exposed to same external compressive stress at given deformation time. Fig. 4.b shows that the WC-Co-Cr requires higher applied compressive stress to reach similar macroscopic strain. Furthermore, comparison with the linear dashed line suggests that yielding takes place earlier (at lower applied stress) in the WC-Co. Stress-strain curves for both samples show instantaneous jumps in the strain values, which are particularly visible in WC-Co-Cr after −0.013 strain. These jumps likely reflect limitations in the macroscopic ETMT strain measurement, such as intermittent grip slippage. In view of the known high-temperature creep behavior of WC–Co, possible contributions from cavitation-related strain localization cannot be excluded. In the following section of the manuscript, S-XRD analysis results provides results for the direct measurements of phase-specific strain and stresses.

Fig. 5 shows a typical S-XRD pattern from the WC-Co cemented carbide acquired at 1000 °C. Despite relatively low binder phase volume fraction in the specimen, S-XRD enables the detection of the first five diffraction peaks, (111), (200), (220), (311), and (222), of FCC Co at 1000 °C, with the (311) peak used for residual stress analysis. In addition, multiple WC diffraction peaks are observed, with the (201) peak used for residual stress analysis, as it is weakly affected by the intergranular strains in HCP materials [29] and thus commonly used for WC [30].

Fig. 6 shows the evolution of stresses along the transverse (σ_X/σ_Y) and loading (σ_Z) directions, as well as the τ_{XZ}/τ_{YZ} shear stresses in the WC phase, for both WC-Co and WC-Co-Cr cemented carbides during high-temperature deformation determined by S-XRD. In the transverse direction (Fig. 6.a), up to about 330 s of straining, where the external compressive stresses exceed 850 MPa, the WC-Co sample develops tensile stresses in WC, whereas WC-Co-Cr sample shows compressive transverse stresses. In the loading direction (Fig. 6.b), both samples are in compression, but the WC-Co-Cr sample consistently shows higher compressive stresses than WC-Co at the same applied load (or deformation time). For example, at an applied strain of −0.01, the difference in applied engineering stress between the two materials is about 150 MPa (Fig. 4b). When the phase-specific WC stress in the loading direction is plotted as a function of applied strain (Fig. 6d), the WC-Co-Cr cemented carbide exhibits about 230 MPa higher compressive WC stress ($\Delta\sigma_{ZZ}$) than the WC-Co sample at the same strain. No significant difference is observed in the shear-stress response of the WC phase between the two materials (Fig. 6c). This is expected as the measured directions correspond to the principal stress axes, where the shear stress is theoretically zero.

Fig. 7 presents the evolution of stresses in the Co-rich binder phase during the high-temperature deformation experiments as determined by S-XRD. In the transverse direction (Fig. 7.a), both samples initially exhibit tensile stresses in the Co-rich binder, which increase with the applied compressive stress. Both samples show similar stresses in X/Y and *Z*-directions. Additionally, the WC-Co-Cr sample maintains slightly higher tensile stress levels up to about 330 s. After this time, the WC-Co sample shifts in the apparent stress state toward more compressive values. Since a similar evolution is also observed in both transverse and loading directions for both phases, this late-stage response is likely influenced by specimen bending or misalignment causing a change in sample-to-detector distance. Therefore, the late-stage phase-specific stress evolution of the WC-–Co sample after about 330 s should be interpreted with caution. In contrast, the WC-Co-Cr sample continues to develop higher tensile stresses until its fracture. In the loading direction (Fig. 7.b), both samples show tensile stresses in the binder phase. Both materials continue accumulating stress under compression until failure while the WC-Co-Cr sample reaches about 250 MPa higher tensile stress than the WC-Co sample. The shear stresses (Fig. 7.c) are of similar

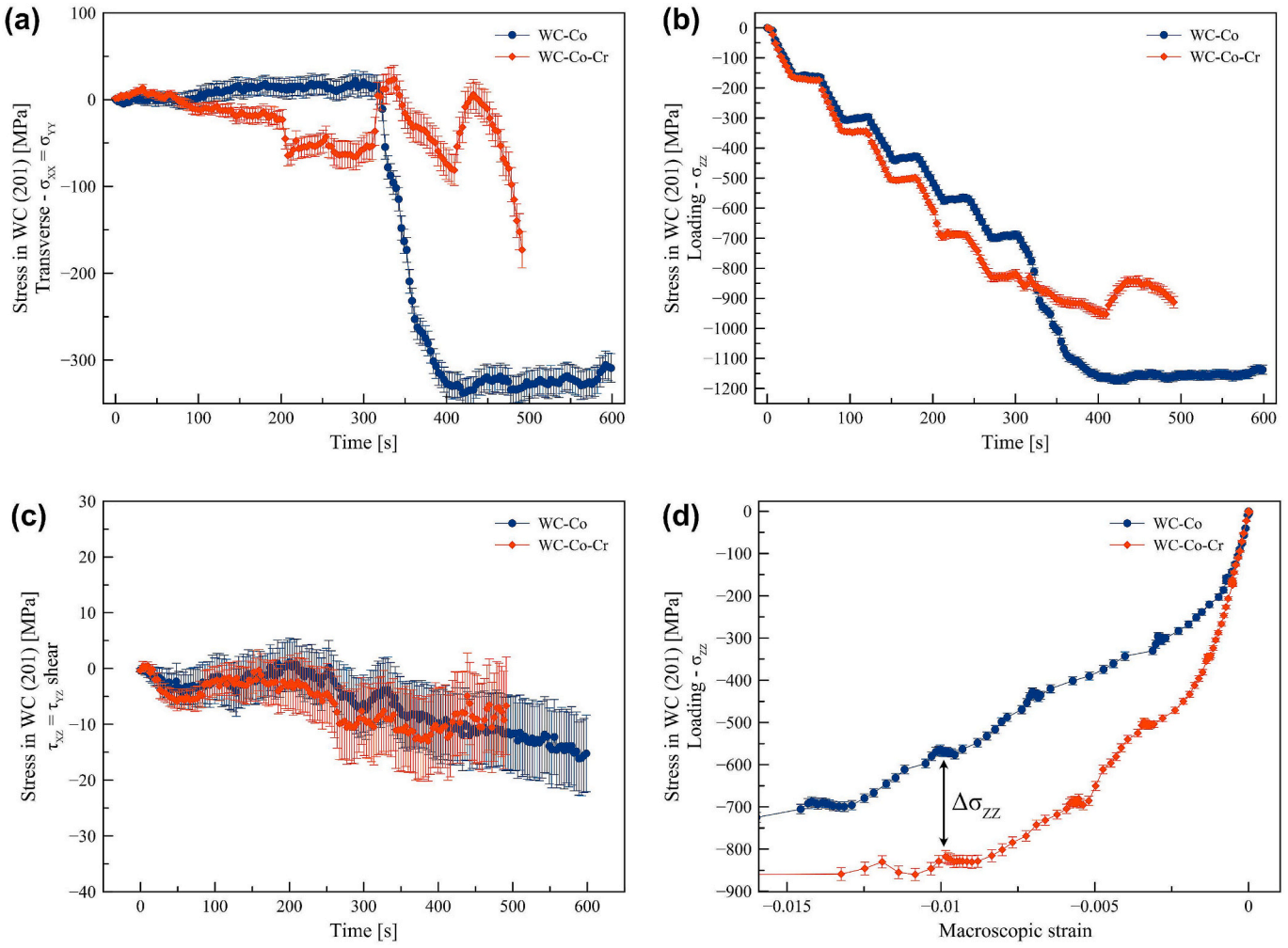

Fig. 6. Evolution of stresses in the transverse (X-Y) (a) and loading (Z) (b) directions, as well as XZ shear stresses (c) in WC phase, for both WC-Co and WC–Co-Cr cemented carbides during deformation at 1000 °C. (d) Stress in the WC phase along the loading direction (Z) plotted as a function of macroscopic strain, showing that WC–Co–Cr exhibits higher compressive WC stress ($\Delta\sigma_{ZZ}$) than WC–Co at the same strain.

magnitude in both materials and remain close to zero, within the calculated uncertainties.

4. Discussion

We here present in-situ experimental results of phase-specific stress evolution in the WC and Co-rich binder phases in WC-Co and WC-Co-Cr cemented carbides under service-relevant temperature and deformation conditions (Figs. 6 and 7), together with the corresponding macroscopic stress–strain response measured by ETMT (Fig. 4). Our results demonstrate that the measured stresses in the Co-rich binder phase satisfy $\sigma_X = \sigma_Y \approx \sigma_Z$ in both WC-Co and WC–Co-Cr cemented carbides (Fig. 7a, b). This suggests that the binder phase experiences a hydrostatic stress state during deformation. In contrast, the WC phase exhibits a more pronounced deviatoric stress state, i.e. stress magnitudes along the transverse (X/Y) and loading (Z) directions differ (Fig. 6a, b). This is an interesting result and leads to the question of what the driver for this type of stress partitioning is. One explanation could be that the binder in the cemented carbide skeleton behaves more like a liquid than a solid. Liquids cannot sustain shear stresses and are therefore always in a hydrostatic stress state. This effect is further amplified by the fact that WC forms the continuous, load-bearing skeleton at a substantial volume fraction, so most externally applied stresses are carried by the WC network while the binder accommodates deformation in a nearly hydrostatic manner. Under such conditions, the stress state in the WC must conform to the physical constraints imposed by the hydrostatic stress distribution in the binder. While WC in WC-Co shows slight tensile stresses and WC in WC-Co-Cr shows slight compressive stresses in the transverse direction (Fig. 6a), both materials exhibit significantly higher compressive stresses in the loading direction (Fig. 6b).

In the WC-Co-Cr material, higher tensile stresses were observed in the binder phase in both loading and transverse directions compared to the WC-Co material (Fig. 7a, b). This suggests that Cr-doping strengthens the Co-rich binder phase, affecting key mechanical properties such as yield strength, strain hardening behavior, and load sharing, i.e. the way load is partitioned between WC and the binder phase. As a result, WC in the WC-Co-Cr sample carries higher compressive stresses along the loading direction, compared to WC in the WC-Co sample (Fig. 6b, d). At an applied strain of about −0.01, the WC-Co-Cr material exhibits approximately 230 MPa higher compressive WC stress in the loading direction than the WC-Co material (Fig. 6d), while the corresponding difference in applied engineering stress is about 150 MPa (Fig. 4b). These observations suggest that Cr-doping modifies the stress partitioning between WC and binder: the binder in the Cr-doped material carries higher hydrostatic tensile stresses while the WC skeleton sustains higher compressive stresses.

Differences in the phase response to compressive loading and load partitioning may impact the binder infiltration between WC grains, cavity formation, and accordingly the WC grain boundary sliding, which are commonly observed mechanisms in high-temperature deformation

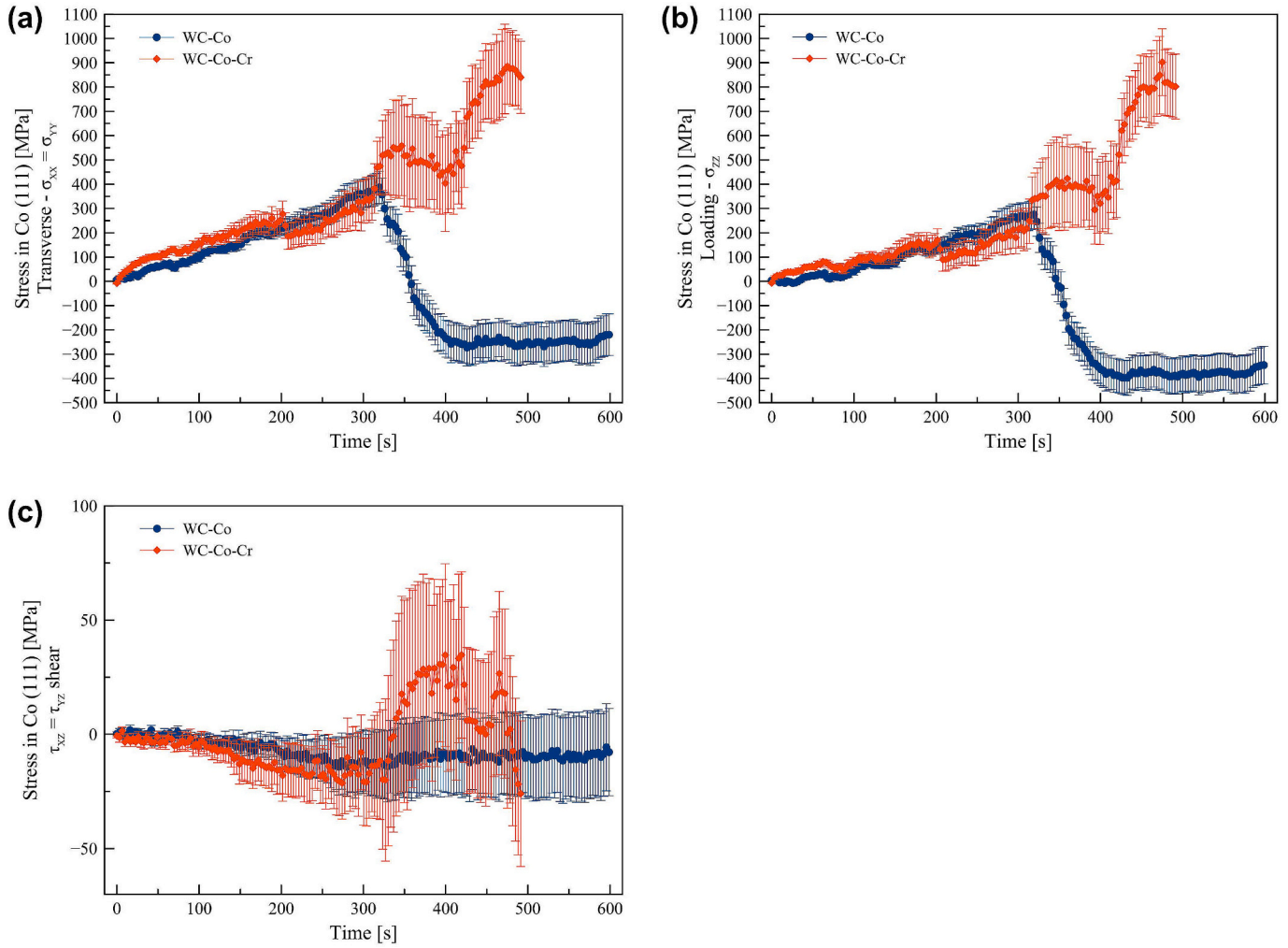

Fig. 7. Evolution of stresses in the transverse (X-Y) (a) and loading (Z) (b) directions, as well as XZ shear stresses (c) in Co-rich binder phase, for both WC-Co and WC–Co-Cr cemented carbides during deformation at 1000 °C.

of cemented carbides [6]. Previous compression creep studies on WC-Co have shown that deformation is associated with binder phase lamella formation and intergranular cavity formation. Such cavity formation suggests that unaccommodated grain boundary sliding also occurs [3,5]. In addition, cavity formation together with Co penetration, often at WC-Co boundaries, has also been reported in high-temperature creep studies, including in interrupted tests prior to final failure [6]. Although no interrupted or post-mortem microstructural analysis was performed in the present work, such cavity formation could also partly contribute to the late-stage stress redistribution observed here (Figs. 6 and 7). Previous studies [3,4,31–33] have reported that Cr-doping modifies the composition of WC/WC and WC/binder interfaces through Cr segregation that promotes the stabilization of metastable cubic (Cr,W)C interfacial layers due to the low interfacial energy of the WC/(Cr,W)C interface. Such interface modifications can strengthen WC/WC boundaries and increase the work of separation relevant for binder infiltration [9,10].

Recent atom probe tomography investigations have also revealed formation of bulk M_7C_3-type Cr precipitates in the as-sintered state at the room temperature [16]. This is also in agreement with the equilibrium thermodynamic predictions at 1000 °C in the present work (Tables 2 and 3). However, no such M_7C_3-type Cr precipitates were observed in our S-XRD patterns, likely due to their very low volume fraction falling below the detection limit. Cr is a well-known WC grain growth inhibitor, whose magnitude depends on the carbon activity of the system [11]. In the present work, however, the materials were designed to exhibit similar WC grain sizes by adjusting the initial WC powder size to compensate for the grain growth inhibition effect of Cr. As a result, EBSD analysis reveals only minor differences between the Cr-doped and undoped materials in terms of WC contiguity and the fraction of Σ2 grain boundaries (Fig. 3, Table 4). The slightly higher binder area fraction observed in the Cr-doped material is consistent with equilibrium thermodynamics predictions. Therefore, these subtle changes in WC contiguity and the fraction of Σ2 grain boundaries in the as-sintered microstructure might not be the primary factors responsible for the improved high-temperature deformation resistance observed in the Cr-doped material in the present study.

Our equilibrium thermodynamic calculations also show that Cr addition significantly increases the solute content in the Co-rich binder, both at the η-phase limit and at the graphite limit (Table 3). However, the calculations will not take formation of interfacial layers into account and how this change the binder composition is still unknown. Nevertheless, an increased concentration of dissolved W and Cr in the binder is expected to strengthen the binder phase through solid-solution hardening. This aligns with our S-XRD stress partitioning results, where the WC–Co–Cr material reaches approximately 250 MPa higher tensile stress in the Co-rich binder before failure compared to the WC–Co material (Fig. 7b). Whereas stronger binder can contribute to increased strength of the WC-Co composite, a higher binder volume fraction is expected to have an adverse effect. Our results suggest that the

strengthening effect associated with increased solute content in the binder dominates over the potentially adverse effect of a higher binder fraction. We further note that the magnitude and governing mechanism of solid solution hardening can change at elevated temperatures due to thermally activated deformation and solute mobility [34]. Together, the enhanced high-temperature deformation resistance observed in the Cr-doped material is likely associated with binder strengthening arising from increased solute content [7] and altered WC/Co and WC/WC interface chemistry, i.e. the formation of interface-stabilized (Cr,W)C interfacial layers.

We propose future studies including small-angle scattering and electron microscopy to gain deeper insights into the role of Cr-doping on the microstructural evolution, including the evolution of interfacial layers and cavity nucleation and growth, as well as on the mechanical performance of cemented carbides. In addition, macroscopic measurement of deformation using the ETMT setup used here could be improved using digital image correlation (DIC), extensometer or strain gauge [14] to minimize uncertainties caused by slipping in the sample grip and improve the accuracy of the absolute strain measurements.

5. Conclusions

This work presents initial in-situ S-XRD investigations of cemented carbides, comparing Cr-doped and un-doped composites, under service-relevant thermomechanical conditions. We demonstrate the applicability of S-XRD in combination with ETMT to study phase-specific deformation behavior of WC and the Co-rich binder phase at 1000 °C under up to 900 MPa uniaxial compressive stress.

Our findings show that Cr-doping affects the mechanical response of both WC and Co-rich binder phases under high-temperature compressive loading. Strengthening of the binder phase in Cr-doped system enables it to sustain higher tensile stresses during deformation, which in turn alters load partitioning between the phases. As a result, the WC phase in the Cr-doped system carries higher compressive stresses and requires approximately 230 MPa higher compressive stress to reach similar macroscopic deformation compared to the un-doped system. These results suggest that Cr-doping redistributes load from the binder to WC skeleton and increases the overall resistance to deformation.

Furthermore, the differences in the phase-specific stress evolution suggest that the improved high-temperature deformation, i.e. creep, resistance in the Cr-doped system is likely associated with solute- and interface-related effects in the binder and altered WC/Co and WC/WC interface chemistry such as the formation of interface-stabilized (Cr,W)C layers, which may affect binder infiltration, WC grain boundary sliding, and microstructural stability.

Further research is proposed to detail the impact of Cr-doping on creep resistance, phase interactions, interfacial layer formation, and deformation mechanisms. These insights will contribute to optimizing the design of high-performance WC–Co cemented carbides for demanding applications such as metal cutting and rock drilling.

CRediT authorship contribution statement

Ahmet Bahadir Yildiz: Writing – original draft, Visualization, Validation, Software, Methodology, Investigation, Formal analysis, Data curation, Conceptualization. **Anna Böhm:** Writing – review & editing, Visualization, Validation, Investigation, Formal analysis, Data curation. **Ida Borgh:** Writing – review & editing, Validation, Investigation, Formal analysis. **Abdalrhaman Koko:** Writing – review & editing, Resources, Methodology. **Christina Reinhard:** Writing – review & editing, Validation, Resources, Methodology. **Štefan Michalik:** Writing – review & editing, Resources, Methodology, Investigation. **Emil Österberg:** Writing – review & editing, Software, Methodology, Investigation, Formal analysis. **Stefan Olovsjö:** Writing – review & editing, Investigation, Conceptualization. **Mikael Kritikos:** Writing – review & editing, Validation, Methodology, Investigation. **Fredrik Lindberg:** Writing – review & editing, Validation, Methodology, Investigation. **Jonathan Weidow:** Writing – review & editing, Validation, Methodology, Investigation. **Susanne Norgren:** Writing – review & editing, Validation, Resources, Conceptualization. **Peter Hedström:** Writing – review & editing, Supervision, Methodology, Conceptualization.

Declaration of competing interest

The authors declare that they have no known competing financial interests or personal relationships that could have appeared to influence the work reported in this paper.

Acknowledgements

This research was partially funded by the Swedish Agency for Innovation Systems, VINNOVA, within the programme “Industrial utilization of neutron and synchrotron light-based technologies in large-scale research infrastructure” (Reference number: 2021-03839). The in-situ S-XRD data was collected at Diamond Light Source under visit MG35930 with the contribution of Instron ETMT rig as part of the Diamond Light Source and The University of Manchester Collaboration.

Data availability

The S-XRD data supporting the findings of this study are available from the corresponding author upon request after the embargo period (3 years from the data acquisition date at the Diamond.

References

[1] A. Nordgren, A. Ekmarker, S. Norgren, A Rock Drill Button, EP 3 274 482 B1, 2016.
[2] J. Östby, L. Toller-Nordström, S. Norgren, Insights into plastic deformation and binder lamella orientation in hardmetal turning inserts, Int. J. Refract. Met. Hard Mater. 103 (2022) 105779, https://doi.org/10.1016/j.ijrmhm.2022.105779.
[3] M.A. Yousfi, A. Nordgren, S. Norgren, J. Weidow, H.-O. Andrén, L.K.L. Falk, Creep of un-doped and Cr-doped WC-co at high temperature and high load, Int. J. Refract. Met. Hard Mater. 117 (2023) 106417, https://doi.org/10.1016/j.ijrmhm.2023.106417.
[4] M.A. Yousfi, S. Norgren, H.-O. Andrén, L.K.L. Falk, Chromium segregation at phase boundaries in Cr-doped WC-co cemented carbides, Mater Charact 144 (2018) 48–56, https://doi.org/10.1016/j.matchar.2018.06.034.
[5] M.A. Yousfi, J. Weidow, A. Nordgren, L.K.L. Falk, H.-O. Andrén, Deformation mechanisms in a WC–co based cemented carbide during creep, Int. J. Refract. Met. Hard Mater. 49 (2015) 81–87, https://doi.org/10.1016/j.ijrmhm.2014.07.016.
[6] K. Mingard, S. Moseley, S. Norgren, H. Zakaria, D. Jones, B. Roebuck, Microstructural observations of high temperature creep processes in hardmetals, Powder Metall. 64 (2021) 97–107, https://doi.org/10.1080/00325899.2021.1877866.
[7] R. Useldinger, U. Schleinkofer, Creep behaviour of cemented carbides — influence of binder content, binder composition and WC grain size, Int. J. Refract. Met. Hard Mater. 62 (2017) 170–175, https://doi.org/10.1016/j.ijrmhm.2016.06.013.
[8] L.-Y. Tian, R. Lizárraga, H. Larsson, E. Holmström, L. Vitos, A first principles study of the stacking fault energies for fcc co-based binary alloys, Acta Mater. 136 (2017) 215–223, https://doi.org/10.1016/j.actamat.2017.07.010.
[9] M. Christensen, G. Wahnström, Strength and reinforcement of interfaces in cemented carbides, Int. J. Refract. Met. Hard Mater. 24 (2006) 80–88, https://doi.org/10.1016/j.ijrmhm.2005.05.010.
[10] G. Östberg, K. Buss, M. Christensen, S. Norgren, H.-O. Andrén, D. Mari, G. Wahnström, I. Reineck, Mechanisms of plastic deformation of WC–co and Ti(C,N)–WC–Co, Int. J. Refract. Met. Hard Mater. 24 (2006) 135–144, https://doi.org/10.1016/j.ijrmhm.2005.04.009.
[11] J. Weidow, S. Norgren, H.-O. Andrén, Effect of V, Cr and Mn additions on the microstructure of WC–co, Int. J. Refract. Met. Hard Mater. 27 (2009) 817–822, https://doi.org/10.1016/j.ijrmhm.2009.02.002.
[12] M. Emmanuel, Z.L. Li, H. Heptinstall, O. Gavalda-Diaz, R. M'saoubi, T. Persson, S. Norgren, T.B. Britton, F. Giuliani, K. Marquardt, Effect of chromium doping on the grain boundary character of WC-co, Int. J. Refract. Met. Hard Mater. 126 (2025) 106954, https://doi.org/10.1016/j.ijrmhm.2024.106954.
[13] M. Emmanuel, O. Gavalda-Diaz, G. Sernicola, R. M'saoubi, T. Persson, S. Norgren, K. Marquardt, T.B. Britton, F. Giuliani, Fracture energy measurement of prismatic plane and Σ2 boundary in cemented carbide, JOM 73 (2021) 1589–1596, https://doi.org/10.1007/s11837-021-04638-6.
[14] B. Roebuck, M. Brooks, A. Pearce, Good Practice Guide for Miniature ETMT Tests, National Physical Laboratory, United Kingdom, 2016. https://www.npl.co.uk/resources/gpgs/miniature-etmt-tests (accessed December 7, 2025).

[15] J.-O. Andersson, T. Helander, L. Höglund, P. Shi, B. Sundman, Thermo-calc & DICTRA, computational tools for materials science, Calphad 26 (2002) 273–312, https://doi.org/10.1016/S0364-5916(02)00037-8.
[16] J. Weidow, A.B. Yildiz, G. Olsson, V. Lilja, S. Sten, I. Borgh, P. Hedström, M. Kritikos, F. Lindberg, E. Coronel, J. Kelleher, D. Mayweg, M. Thuvander, S. Norgren, Residual stresses and microstructure in fine grained cemented carbides doped with Cr and Ti, Int. J. Refract. Met. Hard Mater. 128 (2025) 107005, https://doi.org/10.1016/j.ijrmhm.2024.107005.
[17] H.-O. Andrén, Microstructures of cemented carbides, Mater. Des. 22 (2001) 491–498, https://doi.org/10.1016/S0261-3069(01)00006-1.
[18] F. Bachmann, R. Hielscher, H. Schaeben, Grain detection from 2d and 3d EBSD data—specification of the MTEX algorithm, Ultramicroscopy 111 (2011) 1720–1733, https://doi.org/10.1016/j.ultramic.2011.08.002.
[19] C.-S. Kim, T.R. Massa, G.S. Rohrer, Interface character distributions in WC–co composites, J. Am. Ceram. Soc. 91 (2008) 996–1001, https://doi.org/10.1111/j.1551-2916.2007.02226.x.
[20] T. Persson, M. Schwind, Correlation of WC grain size distribution to hardness and coercivity, in: 18th International Plansee Seminar, Reutte, 2013.
[21] M. Drakopoulos, T. Connolley, C. Reinhard, R. Atwood, O. Magdysyuk, N. Vo, M. Hart, L. Connor, B. Humphreys, G. Howell, S. Davies, T. Hill, G. Wilkin, U. Pedersen, A. Foster, N. De Maio, M. Basham, F. Yuan, K. Wanelik, I12: the joint engineering, environment and processing (JEEP) beamline at diamond light source, J. Synchrotron. Rad 22 (2015) 828–838, https://doi.org/10.1107/S1600577515003513.
[22] Scatterin SaaS data analysis software, 2025. https://saas.scatterin.com/ (Accessed 7 December 2025).
[23] J. Ramirez-Rico, S.-Y. Lee, J.J. Ling, I.C. Noyan, Stress measurement using area detectors: a theoretical and experimental comparison of different methods in ferritic steel using a portable X-ray apparatus, J. Mater. Sci. 51 (2016) 5343–5355, https://doi.org/10.1007/s10853-016-9837-3.
[24] M. Lee, R.S. Gilmore, Single crystal elastic constants of tungsten monocarbide, J. Mater. Sci. 17 (1982) 2657–2660, https://doi.org/10.1007/BF00543901.
[25] J. Gump, H. Xia, M. Chirita, R. Sooryakumar, M.A. Tomaz, G.R. Harp, Elastic constants of face-centered-cubic cobalt, J. Appl. Phys. 86 (1999) 6005–6009, https://doi.org/10.1063/1.371647.
[26] R.R. Reeber, K. Wang, Thermophysical properties of α-tungsten carbide, J. Am. Ceram. Soc. 82 (1999) 129–135, https://doi.org/10.1111/j.1151-2916.1999.tb01732.x.
[27] M. Mårtensson, S. Norgren, Impact of Chromium on the Magnetic Properties of WC-co Hardmetals, , in: European Congress and Exhibition on Powder Metallurgy. European PM Conference Proceedings,, The European Powder Metallurgy Association, 2016, pp. 1–7, https://search.proquest.com/openview/c60b050517f7a1159f4a0b69e8ef1173/1?pq-origsite=gscholar&cbl=596295 (accessed December 7, 2025)..
[28] J. Weidow, H.-O. Andrén, Binder phase grain size in WC–co-based cemented carbides, Scr. Mater. 63 (2010) 1165–1168, https://doi.org/10.1016/j.scriptamat.2010.08.025.
[29] M.T. Hutchings, P.J. Withers, T.M. Holden, T. Lorentzen, Introduction to the characterization of residual stress by neutron diffraction, CRC press, Boca Raton, 2005, https://doi.org/10.1201/9780203402818.
[30] K. Seol, A.D. Krawitz, Anisotropic residual stress relaxation in cemented carbide composites, Mater. Sci. Eng. A 127 (1990) 1–5, https://doi.org/10.1016/0921-5093(90)90183-4.
[31] T. Yamamoto, Y. Ikuhara, T. Watanabe, T. Sakuma, Y. Taniuchi, K. Okada, T. Tanase, High resolution microscopy study in Cr3C2-doped WC-co, J. Mater. Sci. 36 (2001) 3885–3890, https://doi.org/10.1023/A:1017953701641.
[32] A. Delanoë, M. Bacia, E. Pauty, S. Lay, C.H. Allibert, Cr-rich layer at the WC/co interface in Cr-doped WC–co cermets: segregation or metastable carbide? J. Cryst. Growth 270 (2004) 219–227, https://doi.org/10.1016/j.jcrysgro.2004.05.101.
[33] J. Weidow, H.-O. Andrén, Grain and phase boundary segregation in WC–co with small V, Cr or Mn additions, Acta Mater. 58 (2010) 3888–3894, https://doi.org/10.1016/j.actamat.2010.03.038.
[34] H. ur Rehman, K. Durst, S. Neumeier, A. Sato, R. Reed, M. Göken, On the temperature dependent strengthening of nickel by transition metal solutes, Acta Mater. 137 (2017) 54–63, https://doi.org/10.1016/j.actamat.2017.05.038.